

Article

Photocatalytic Reduction of Cr (VI) over g-C₃N₄ Photocatalysts Synthesized by Different Precursors

Juan Liang ^{1,2}, Chengjun Jing ^{1,2,*} , Jiarong Wang ¹ and Yupawang Men ¹

¹ College of Architecture and Environment, Sichuan University, Chengdu 610065, China; ilyq1119@163.com (J.L.); wjrscu@163.com (J.W.); 18988222020@163.com (Y.M.)

² Institute for Disaster Management and Reconstruction, Sichuan University, Chengdu 610065, China

* Correspondence: chengjunjing@126.com; Tel.: +86-18980892979

Abstract: Graphitic carbon nitride (g-C₃N₄) photocatalysts were synthesized via a one-step pyrolysis process using melamine, dicyandiamide, thiourea, and urea as precursors. The obtained g-C₃N₄ materials exhibited a significantly different performance for the photocatalytic reduction of Cr(VI) under white light irradiation, which is attributed to the altered structure and occupancies surface groups. The urea-derived g-C₃N₄ with nanosheet morphology, large specific surface area, and high occupancies of surface amine groups exhibited superior photocatalytic activity. The nanosheet morphology and large surface area facilitated the separation and transmission of charge, while the high occupancies of surface amine groups promoted the formation of hydrogen adsorption atomic centers which were beneficial to Cr(VI) reduction. Moreover, the possible reduction pathway of Cr(VI) to Cr(III) over the urea-derived g-C₃N₄ was proposed and the reduction process was mainly initiated by a direct reduction of photogenerated electrons.



Citation: Liang, J.; Jing, C.; Wang, J.; Men, Y. Photocatalytic Reduction of Cr (VI) over g-C₃N₄ Photocatalysts Synthesized by Different Precursors. *Molecules* **2021**, *26*, 7054. <https://doi.org/10.3390/molecules26227054>

Academic Editors: Shaojun Yuan, Ying Liang, Changkun Liu and Xiaoying Liu

Received: 29 October 2021

Accepted: 20 November 2021

Published: 22 November 2021

Publisher's Note: MDPI stays neutral with regard to jurisdictional claims in published maps and institutional affiliations.



Copyright: © 2021 by the authors. Licensee MDPI, Basel, Switzerland. This article is an open access article distributed under the terms and conditions of the Creative Commons Attribution (CC BY) license (<https://creativecommons.org/licenses/by/4.0/>).

Keywords: Cr (VI) reduction; photocatalytic; g-C₃N₄ precursors; nanosheet morphology; surface characteristics

1. Introduction

In recent years, with the rapid development of mining, electroplating, leather tanneries, and pigments, a large number of heavy metal compounds have been discharged. Among of them, hexavalent chromium Cr(VI) is one of the most virulent contaminants which can be accumulated by digestion system via the exposure and intake the polluted substance, causing serious illness such as cancer and skin allergy [1–3]. Because of its high toxicity, Cr(VI) has been ranked among the top 20 toxic pollutants on Superfund Priority List of Hazardous Substances [4]. Photocatalytic reduction technology is an attractive alternative technology for Cr(VI) reduction because of its acceptable cost, easy operation, and high safety. Specifically, it can directly reduce high toxic Cr(VI) to less harmful Cr(III), which is a necessary trace element for human being and easy to precipitation in aqueous solution ($K_{sp}^{\theta}(\text{Cr}(\text{OH})_3) = 6.3 \times 10^{-31}$) [5–7].

As a metal-free semiconductor photocatalyst, graphitic carbon nitride (g-C₃N₄) has been widely studied due to its visible-light-driven, narrow bandgap, non-toxic, low cost, and excellent stability [8,9]. In addition, the conduction band of g-C₃N₄ level is much more negative than that of Cr(VI)/Cr(III) (1.3 eV vs. NHE), suggesting that the photo-generated electrons in g-C₃N₄ possess a large thermodynamic driving force to reduce Cr(VI) to Cr(III) [10,11]. In general, g-C₃N₄ can be synthesized via thermolysis method from cheap available nitrogen-rich precursors such as urea, thiourea, cyanamide, dicyandiamide, and melamine. Due to the different chemical structures of these nitrogen-rich precursors, as well as the influence of foreign chemical elements such as O and S, the g-C₃N₄ photocatalysts prepared from these nitrogen-rich precursors exhibit different structural and optical properties, and thus display different photocatalytic activities [12–14].

Several studies have been conducted to investigate the effect of various precursors on photocatalytic performance and the characteristics of $g\text{-C}_3\text{N}_4$. However, the field of application of $g\text{-C}_3\text{N}_4$ derived from diverse precursors is debatable in these studies. Tian et al. found that urea-derived $g\text{-C}_3\text{N}_4$ exhibits superior photocatalytic activity for tetracycline degradation under visible light when compared with thiourea and dicyandiamide [15]. Tim et al. found thiourea served as the best water-dispersible photocatalyst for MB degradation [16]. Guan et al. founded that $g\text{-C}_3\text{N}_4$ synthesized from melamine and annealed in N_2 exhibited much higher catalytic activities for PMS activation rather than urea or thiourea [17]. Furthermore, the correlation between the catalytic activities and the properties $g\text{-C}_3\text{N}_4$, such as structure, morphology, photochemical, and electrochemical properties is frequently incomplete [18]. Martha et al. found the charge separation property is more relevant than the specific area in the photocatalytic hydrogen evolution [19], while Martin et al. showed the large surface area and porous structure are the main factors for the high hydrogen evolution rate [20]. Ismael et al. claimed that $g\text{-C}_3\text{N}_4$ with a low polymerization degree has greater photocatalytic activity [21], while Ibad et al. claim that high crystallinity combined with mesoporosity yield highest active $g\text{-C}_3\text{N}_4$ [22]. Therefore, understanding the impacts of different precursors on the photocatalytic reduction of Cr(VI) and the characteristics of $g\text{-C}_3\text{N}_4$ will be useful for rationally designing of $g\text{-C}_3\text{N}_4$ with good photocatalytic performance.

Until now, most of the investigations on photocatalytic reduction of Cr(VI) have focused on the modification of $g\text{-C}_3\text{N}_4$ material itself, such as copolymerization [23], exfoliation [24], doping [25], heterostructure fabrication [26], etc. There have been few studies on the impact of using various nitrogen-rich precursors. In this paper, $g\text{-C}_3\text{N}_4$ photocatalysts were synthesized via a thermal polymerization technique with dicyandiamide, melamine, thiourea, and urea as precursors. The obtained products were named as D-CN, M-CN, T-CN, and U-CN, respectively. The resulting catalysts' structure, morphology, surface properties, photoelectrochemical properties, and the photocatalytic reduction performance of Cr(VI) were further investigated. It was found that urea-derived $g\text{-C}_3\text{N}_4$ (U-CN) exhibits the highest activity due to the nanosheet morphology, large specific surface area, and high occupancies of surface amine groups. Further, these results demonstrate that the specific surface area and surface characteristics play a more predominant role in influencing photocatalytic reduction of Cr(VI) than the photoelectronic properties. Finally, a putative Cr(VI) to Cr(III) reduction pathway in U-CN was hypothesized.

2. Results and Discussion

2.1. Structure and Morphology

Figure 1a shows X-ray diffraction (XRD) patterns of $g\text{-C}_3\text{N}_4$ prepared by different precursor systems. It can be seen from the XRD pattern that the $g\text{-C}_3\text{N}_4$ obtained by the four precursors all have two characteristic peaks. The weak peak near 12.8° is attributed to intralayer long-range atomic order (100), which is associated with the hydrogen bonds in $g\text{-C}_3\text{N}_4$ [27,28]. The stronger peak near 27.4° corresponded to the (002) crystal plane of $g\text{-C}_3\text{N}_4$, which is caused by the interlayer accumulation of the conjugated aromatic system [29]. These characteristic diffraction peaks are consistent with previous reports. In addition, the diffraction peaks of U-CN are broader and lower intensity, indicating that U-CN has the lowest crystallinity. The low crystallinity of U-CN might be that extra O in urea produces H_2O , CO_2 , and ammonia during calcination, which inhibit the growth of the surface crystal [30]. Furthermore, the (100) crystal plane of U-CN is substantially lower than the other three samples, indicating a reduced hydrogen bond effect in the intralayer of U-CN [20].

Figure 1b presents the FTIR spectra of the $g\text{-C}_3\text{N}_4$ samples to demonstrate their graphitic structures. The absorption peaks observed between $1200\text{--}1700\text{ cm}^{-1}$ correspond to the characteristic breathing modes of aromatic carbon nitride heterocyclic rings [31]. The sharp absorption band at around 801 cm^{-1} is attributed to the respiratory pattern of triazine units while the board vibration bands at $3000\text{--}3500\text{ cm}^{-1}$ can be ascribed to

the uncondensed amine groups and the water molecules adsorbed on the surface [14]. In addition, it can be seen from Figure 1c that U-CN blue-shifted at 801 cm^{-1} . The main reason might be due to the hydrogen bond-containing which influences the triazine ring stretching in the $g\text{-C}_3\text{N}_4$ structure [16].

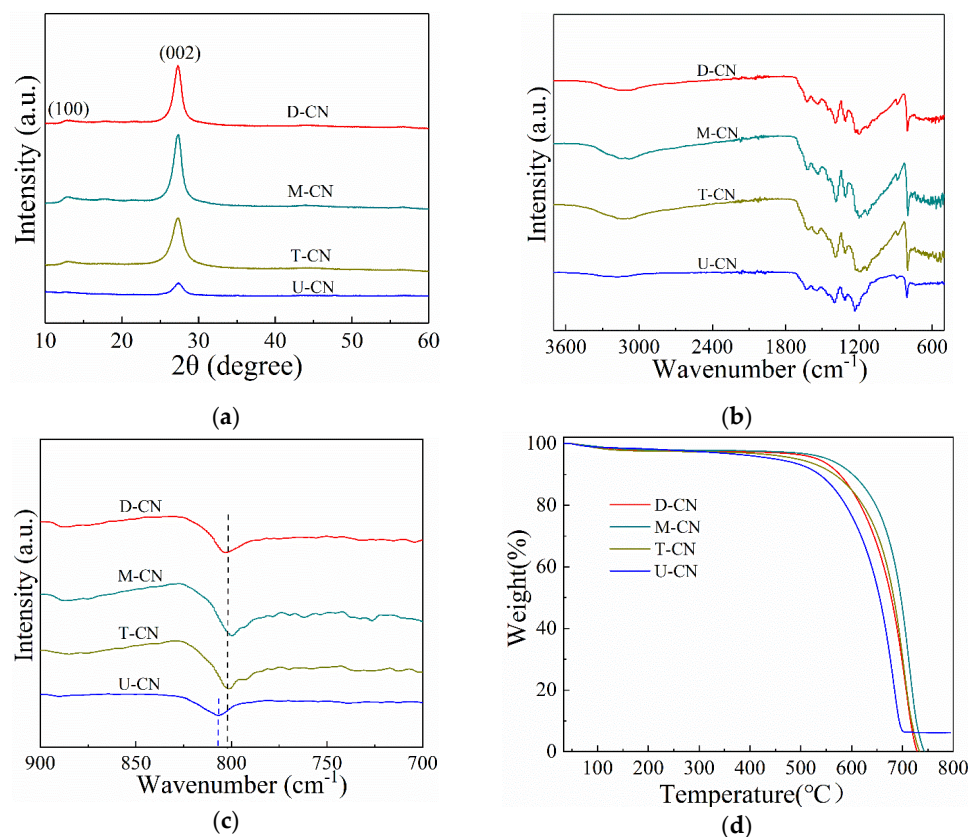


Figure 1. (a) XRD patterns; (b) FT-IR spectra; (c) partial enlarged FT-IR spectra, and (d) TG curves of $g\text{-C}_3\text{N}_4$ prepared by different materials.

The lower degree of polymerization of U-CN can also be obtained from thermal stability of the different as-prepared $g\text{-C}_3\text{N}_4$. It can be seen from Figure 1d that there is no further significant weight loss up to a temperature of $400\text{ }^\circ\text{C}$. However, weight losses of 21.1%, 29.0%, 33.3%, and 53.5% were observed for the M-CN, T-CN, D-CN, and U-CN between $400\text{ }^\circ\text{C}$ to $650\text{ }^\circ\text{C}$, respectively. U-CN can be completely decomposed at $700\text{ }^\circ\text{C}$, while the completely decomposition temperature of T-CN, D-CN, and M-CN are $728\text{ }^\circ\text{C}$, $732\text{ }^\circ\text{C}$, and $746\text{ }^\circ\text{C}$, respectively. The result suggest that U-CN has the worst thermally stability, which might be due to its low degree of polymerization and poor stability of the triazine ring structure.

The morphologies of the prepared samples were investigated by SEM. D-CN and M-CN show the typical flat and layered structure with small lamellas wrapped in large particles (Figure 2a,b), whereas T-CN has an obvious layered structure, with large lamellae and a few fine particles scattered on the surface (Figure 2c). U-CN displays nanosheets morphology with irregular wrinkles (Figure 2d) [32]. It can also be observed that U-CN displays porous structure while the last three sample present large sheet without porous structures.

The surface area and porous structure of the prepared samples were further studied on the basis of nitrogen gas adsorption–desorption isotherms and pore size distribution curves. As shown in Figure 3, all the samples exhibit a classical type IV isotherms, which is the characteristic of the typical mesoporous materials. The BET surface areas and pore volume of the as-prepared samples were summarized in Table 1. It can be seen that U- $g\text{-C}_3\text{N}_4$ has the largest specific surface area ($S_{\text{BET}} = 81.060\text{ m}^2\text{ g}^{-1}$) and pore volume ($V_{\text{meso}} = 0.164\text{ cc g}^{-1}$), while the

BET surface areas and pore volume of D-CN ($S_{\text{BET}} = 8.779 \text{ m}^2 \text{ g}^{-1}$, $V_{\text{meso}} = 0.025 \text{ cc g}^{-1}$), M-CN ($S_{\text{BET}} = 8.363 \text{ m}^2 \text{ g}^{-1}$, $V_{\text{meso}} = 0.021 \text{ cc g}^{-1}$), and T-CN ($S_{\text{BET}} = 7.262 \text{ m}^2 \text{ g}^{-1}$, $V_{\text{meso}} = 0.019 \text{ cc g}^{-1}$) have little difference. These results are in good agreement with the morphologies of the samples. The presence of the oxygen heteroatom in urea might also play an important role in increasing the BET surface area and pore volume of the U-CN sample. The emission of pyrolysis-generated gases during the thermal condensation process can function as soft templates and promote the formation of porous structure [33,34]. The external surface area is very important in photocatalytic action as the reactions take place mainly on the external surface that is exposed to light irradiation.

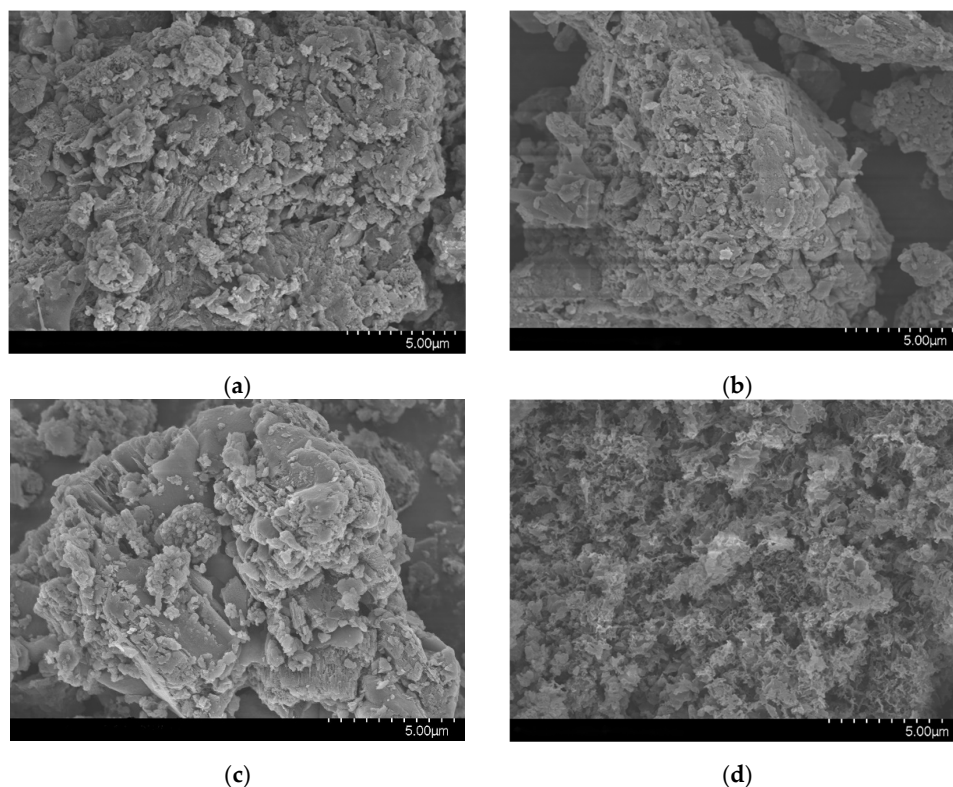


Figure 2. SEM of $\text{g-C}_3\text{N}_4$: (a) D-CN, (b) M-CN, (c) T-CN, and (d) U-CN.

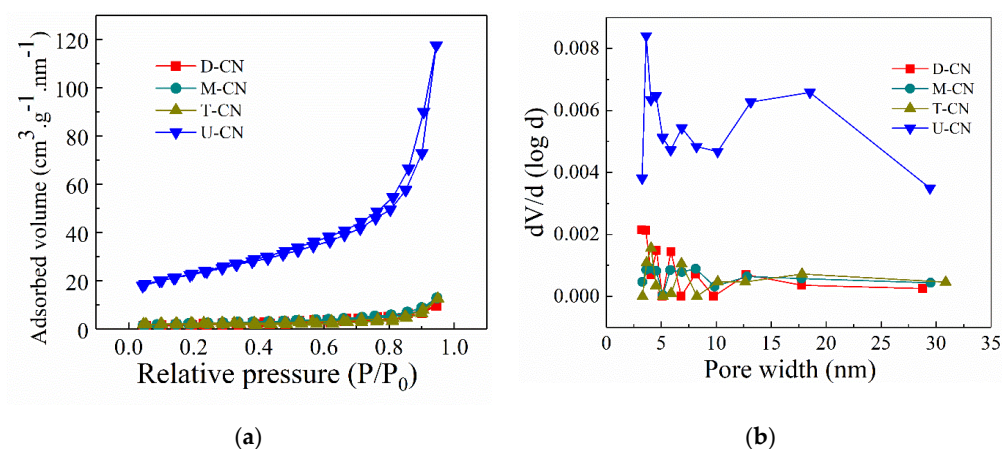
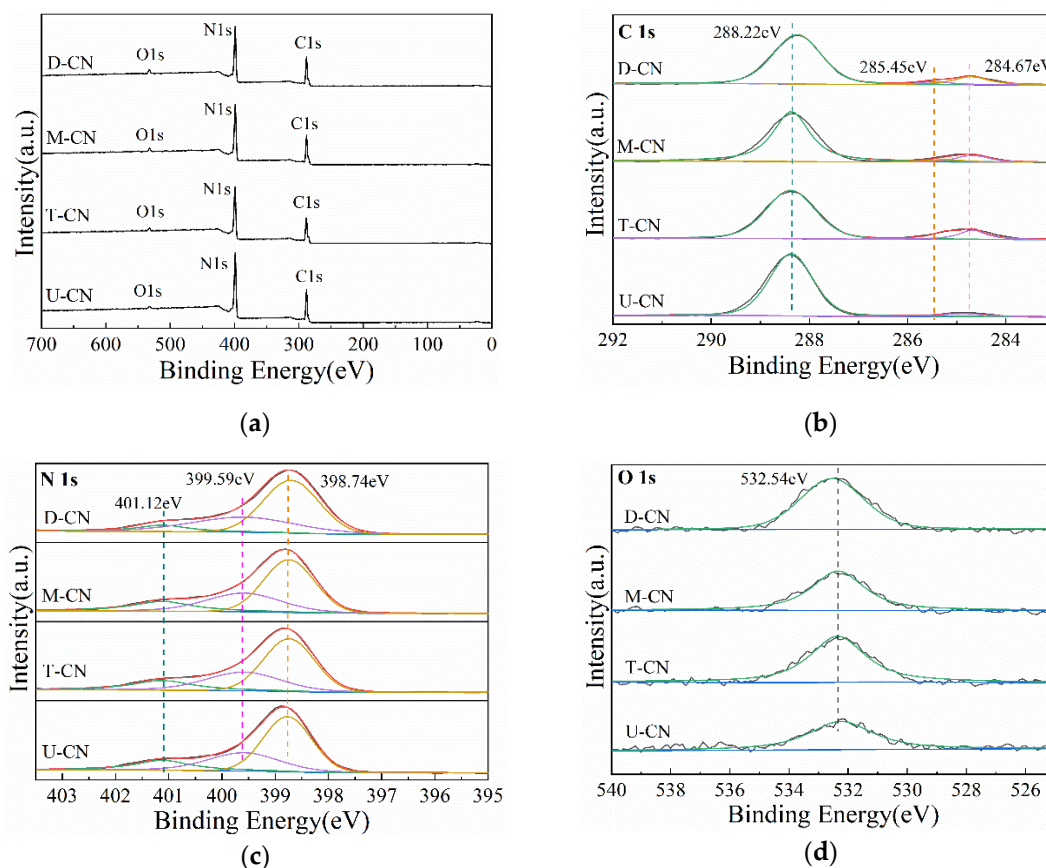


Figure 3. (a) N_2 adsorption-desorption isotherms and (b) corresponding pore size distribution curves of D-CN, M-CN, T-CN, U-CN.

Table 1. Specific surface area and pore volume of as-prepared samples.

Name	BET (m ² g ⁻¹)	Pore Volume (cc g ⁻¹)	Elemental Composition (wt%)				Zeta Potential (mV)	E _{gap} (eV)	k (min ⁻¹)
			C	N	O	C/N			
D-CN	8.779	0.025	43.85	53.12	2.86	0.82	-21.45	2.72	0.0285
M-CN	8.363	0.021	43.82	53.94	2.24	0.81	-21.75	2.70	0.0287
T-CN	7.262	0.019	45.13	52.19	2.63	0.86	-23.31	2.68	0.0171
U-CN	81.060	0.164	41.58	56.98	1.44	0.72	-15.13	2.84	0.0822

The XPS spectra of the samples are presented in Figure 4. The survey scan XPS spectra shown in Figure 4a illustrates that the obtained g-C₃N₄ samples are composed of C, N, and O elements. It can also be seen from Figure 4 that C1s, N1s, and O1s have no obvious energy shifts while core electrons occur, indicating the chemical states of the three elements are the same in D-CN, M-CN, T-CN, and U-CN. As shown in Figure 4b, the high-resolution XPS spectra of the C 1s for the samples can be deconvoluted into three peaks with binding energies of 284.67 eV, 285.45 eV, and 288.22 eV, which are characteristic of the sp² C-C bond, C-O bond, and N-C=N bond, respectively [35]. The high-definition N 1s spectra of the samples can be fitted into three distinct peaks at 398.74 eV, 399.59 eV, and 401.12 eV, corresponding to C-N=C, tertiary nitrogen N-(C)₃ and -NH₂ (Figure 4c) [36]. In addition, a weak energy peak at 532.54 eV can also be observed in the high resolution XPS spectra of O1s, which can be attributed to adsorbed H₂O on the sample surface [37] (Figure 4d).

**Figure 4.** XPS spectra of the samples: (a) survey, (b) C1s, (c) N1s, and (d) O1s.

The surface elements content of the samples can be analyzed from the integrated peak areas under C1s, N 1s, and O 1s (Table 1). The atomic ratios of C/N of D-CN, M-CN, T-CN and UCN are determined to be 0.82, 0.81, 0.86, and 0.72, respectively. The C/N ratio of U-CN is the lowest, implying a more defective structure and lower polymerization. The zeta potentials of the samples were measured to investigate the surface charges of the samples. In the suspension with the initial pH, the zeta potentials of D-CN, M-CN, T-CN, and U-CN are -21.45 eV, -21.75 eV, -23.31 eV, and -15.13 eV, respectively. g-C₃N₄ contains abundant Lewis acid and base sites, which are derived from the terminal and bridging NH-groups and lone pairs of N in triazine/heptazine rings, respectively. Amine groups can act as proton acceptors and acquire positive surface charges. Additionally, hydroxyl ions can react with primary and secondary amine groups to produce negative charges on the surface of g-C₃N₄. The surface charges and zeta potentials of g-C₃N₄ are determined by the number of amine groups on the carbon surface and the pH value of the suspension [38]. The amine groups on the U-CN surface are substantially higher than those on the D-CN, M-CN, and T-CN because of the huge specific surface area and much higher surface N element concentration, resulting in a much stronger ability to adsorb hydrogen ions in the solution with the same pH value. Furthermore, Lewis acid and base sites on the surface of g-C₃N₄ are potential anchoring sites for cocatalysts [39]. A higher occupation of surface amine group may provide more active sites for the photocatalytic reaction.

2.2. Photocatalytic Performance

The photocatalytic reduction performance of Cr(VI) over the as-prepared photocatalysts were evaluated under white light irradiation. As shown in Figure 5a, due to the weak electrostatic attraction between the anionic chromate species (HCrO_4^- and/or $\text{Cr}_2\text{O}_7^{2-}$) and the negative charge on the surface of the g-C₃N₄ catalysts, all the samples show poor adsorption capacity for Cr(VI). Under the irradiation of white light, all the samples display significantly different photocatalytic performance, in which U-CN exhibits the best Cr(VI) reduction activity with efficiency of 99.5% within 60 min, while the efficiencies are 71.1%, 74.1%, and 30.7% for D-CN, M-CN, and T-CN, respectively. Figure 5b depicts the kinetic curves of the photocatalytic reduction of Cr(VI) with the typical pseudo-first-order model ($\ln C/C_0 = -kt$). The rate constants of U-CN, D-CN, M-CN, and T-CN are 0.0822 min^{-1} , 0.0285 min^{-1} , 0.0287 min^{-1} , and 0.0171 min^{-1} , respectively. Obviously, U-CN possesses the highest rate constant, which corresponds to the best photocatalytic performance.

Combined with the previous morphological structure and surface characteristics analyses, it was found that the photocatalytic reduction effect of the catalyst has a certain correspondence with its specific surface area. As shown in Figure 5c, a close correlation was found between the C/C_0 and S_{BET} with a correlation coefficient 0.7967. U-CN with nanosheet morphology, large specific surface area has the best photocatalytic reduction performance. The large surface area facilitates the separation and transfer of photoinduced charges in U-CN, as well as provide more active sites for Cr(VI) reduction. In addition, it is worth noting that, despite having a similar surface area as D-CN and M-CN, T-CN had the lowest photocatalytic reduction activity. By analyzing the surface characteristics of the three samples, it is found that the surface amine group content of the samples has a significant impact on the photocatalytic activity. The surface amine groups can act as exciton dissociation traps which are conducive to the rapid splitting of photogenerated excitons and promote the formation of hydrogen adsorption atomic centers, thus facilitating the photocatalytic reduction of Cr(VI) [39]. The effect of S_{BET} is excluded while investigating the possible role of surface amino groups in the photocatalytic reduction process. Figure 4d shows the association between normalized C/C_0 ($(C/C_0)/S_{\text{BET}}$) and zeta potential. As illustrated in Figure 4d, the value of normalized C/C_0 is closely correlation with the zeta potential which is determined by the varied specific area and the occupation of the surface amine groups [38]. The correlation coefficient is conculcated to be 0.8686. The results reveal that the photocatalytic reduction activity of Cr(VI) is affected by the specific

surface area and the amount of surface amine groups, and the amount of surface amine groups has a greater impact.

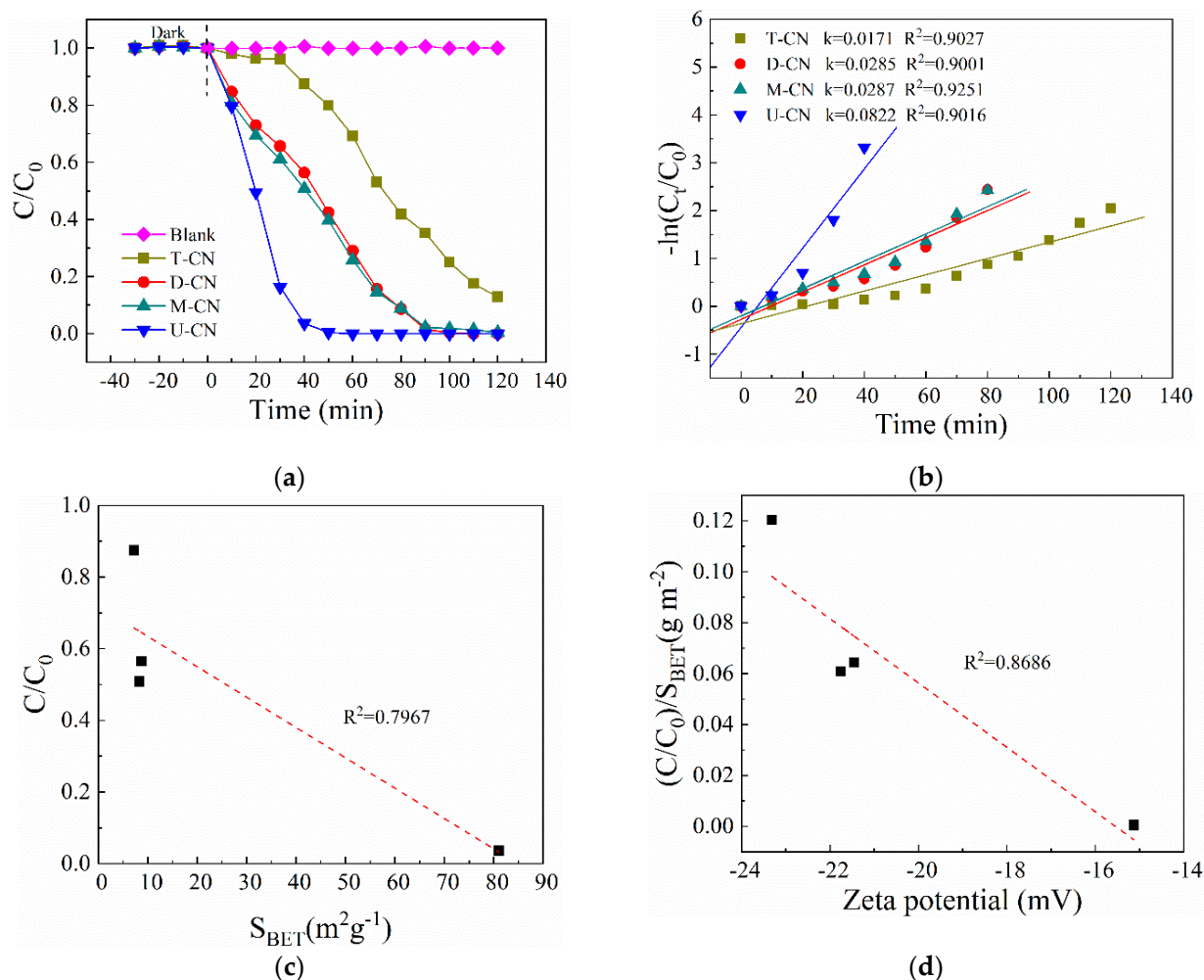
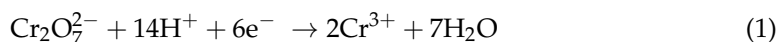


Figure 5. (a) Effect of materials on the photocatalytic activity of $g\text{-C}_3\text{N}_4$, (b) Photodegradation kinetic constants of $g\text{-C}_3\text{N}_4$ prepared from different materials, (c) Correlation of C/C_0 and specific surface area (S_{BET}), (d) Correlation of N content and normalized C/C_0 (k/S_{BET}). (Experimental conditions: initial Cr(VI) concentration = 50 mg L^{-1} ; catalyst amount = 50 mg ; reaction volume = 150 mL ; citric acid = 0.9 Mm ; $\text{pH} = 3$; white light irradiation).

Figure 6a depicts the effect of initial pH of the solution on Cr(VI) reduction over U-CN. The photocatalytic reduction efficiency of Cr(VI) decreases markedly with the increase of pH value. In addition, when pH is 7 or 9, Cr(VI) cannot be degraded at all. pH value affects the existence of Cr(VI) as well as the surface charge of $g\text{-C}_3\text{N}_4$. Cr(VI) is presented as $\text{Cr}_2\text{O}_7^{2-}$, HCrO_4^- in acidic solution and mainly as CrO_4^{2-} in basic solution [40]. The surface of the catalyst becomes highly protonated at low pH value, which makes the surface of the catalytic more conducive to the accumulation of HCrO_4^- . While the surface of $g\text{-C}_3\text{N}_4$ is negatively charged at alkaline solution, which tends to repel the $\text{Cr}_2\text{O}_7^{2-}$. The Cr(VI) photoreduction was achieved following Equations (1) and (2) under acidic solution, and the hydrogen ion was beneficial to the reduction reaction. In contrast, the Cr(VI) reduction under alkaline solution was accomplished following Equation (3) [41]. In addition, $\text{Cr}(\text{OH})_3$ may be formed under high pH value and covers the active sites of the photocatalyst, leading to the declining Cr(VI) reduction performance [42].



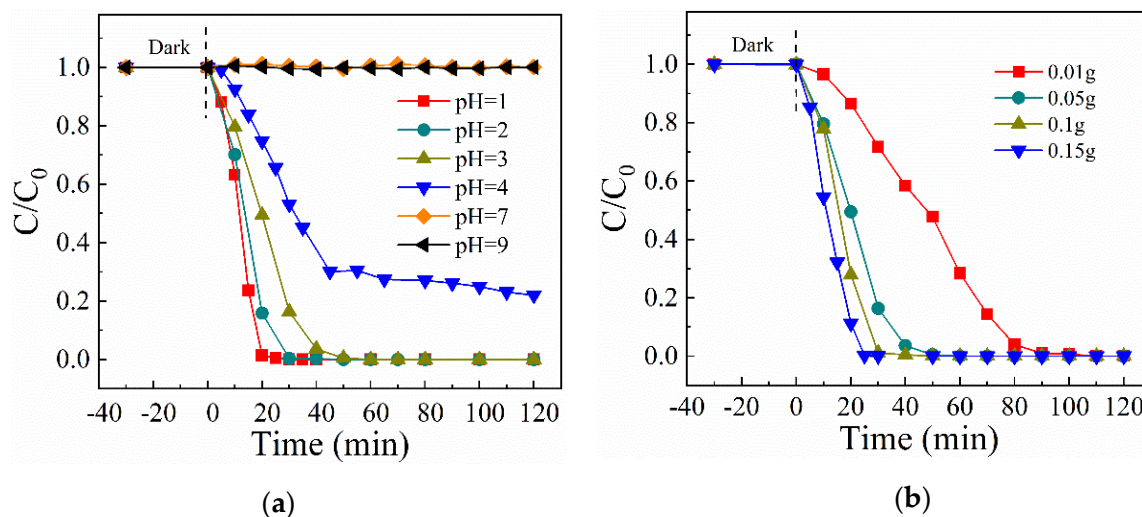
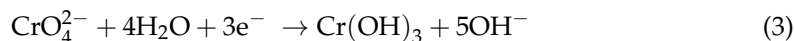
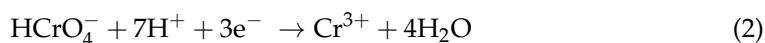


Figure 6. Effect of (a) initial pH and (b) U—CN dosage on photocatalytic Cr(VI) reduction (Vary conditions are based on the control experiment: Cr(VI) = 50 mg/L; U—CN mount = 50 mg; reaction volume = 150 mL; citric acid = 0.9 Mm; pH = 3; white light irradiation).

The effect of U—CN dosage was also tested. As shown in Figure 6b, the photocatalytic reduction rate of Cr(VI) increases dramatically as the amount of U—CN catalyst is increased. The improvement in the photocatalytic degradation rate of Cr(VI) declined as the catalyst dosage was increased further. The reason might be that the effect of photocatalytic reaction is related to the catalyst surface's reaction sites [26]. The catalyst's reaction sites can be effectively increased by increasing the catalyst dosage. While the surface active sites meet the need for Cr(VI) reduction as the dose is increased, the influence of the catalyst dosage on the total reaction rate of Cr(VI) reduction is lowered.

Furthermore, the Influencing factors on Cr(VI) photocatalytic reduction including light sources, hole scavengers, initial Cr(VI) concentration are presented in Supplementary Material (Figures S2–S4).

2.3. Photoelectrochemical Properties

Figure 7a shows the UV-visible absorption spectra of the samples. T—CN exhibits stronger light absorption in the range of 400 to 700 nm than that of the other three samples. While the absorption edge of U—CN showed a significant blue shift with respect to the other three samples [16,21]. The band-gap energies of the samples are calculated by plots of $(\alpha h\nu)^{1/2}$ versus photo energy. As depicted in Figure 7b, the bandgaps of T—CN, M—CN, D—CN and U—CN are estimated to be 2.68, 2.70, 2.72 and 2.84 eV, correspondingly. U—CN has a larger band gap might be attributed to the quantum size effect caused by smaller and disordered crystalline domains [33,34]. The band structures of the samples were further characterized by valence band XPS(VB-XPS). As shown in Figure 7c, the VB maxima of D—CN, M—CN, U—CN and T—CN are 2.22, 2.22, 2.28 and 2.32 eV, respectively [43]. According to the results of UV-DRS spectra and CB XPS, the VB potential of D—CN, M—CN, T—CN and U—CN are conculcated to be -0.50 , -0.48 , -0.56 , -0.36 eV, respectively. Due to the most negative CB potential in UCN, the photogenerated electrons produced by U—CN have the most reducing ability for Cr(VI) reduction in comparison to those in the other three samples.

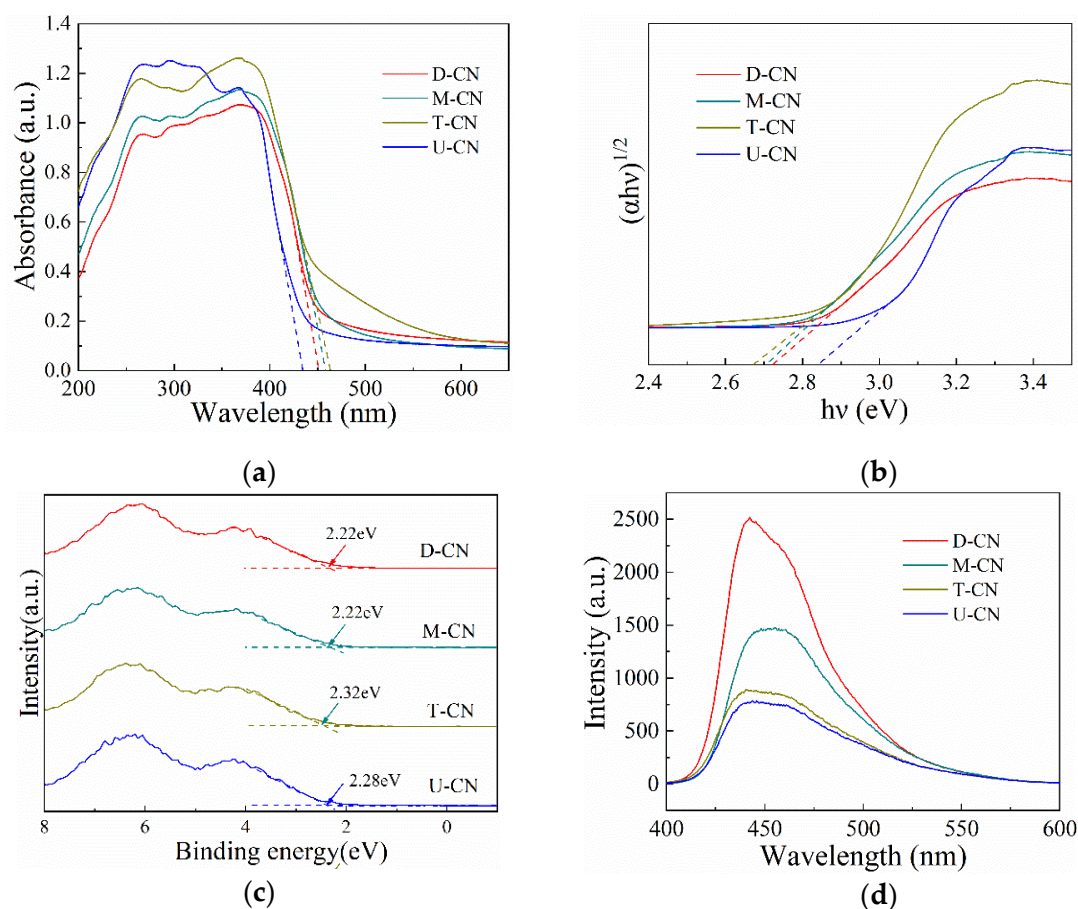


Figure 7. (a) UV-vis DRS spectra; (b) Tauc plots for estimating the bandgap (E_g) values (c) XPS valence band (VB) spectra and (d) band structure of D-CN, M-CN, T-CN and U-CN.

The transfer behavior and separation efficiency of photogenerated charge carriers in the samples can be reflected by the photoluminescence (PL) spectra. As shown in Figure 7d, the emission peak centers of the four samples are around 440 nm, which represented the irradiative recombination of e^- and h^+ [21]. The emission intensity is lower for the U-CN as compared to the other three samples, indicating the recombination rate of electrons and holes under white light irradiation is lower in U-CN. To further investigate the separation efficiency of photogenerated charges during the photoreactions, photoelectrochemical measurements were performed. As displayed in Figure 8a, fast photocurrent responses via on-off cycles were observed for all the samples, while the photocurrent intensity of U-CN was obviously higher than that of the other three samples. In addition, the arc radius of U-CN in the EIS Nyquist plot shown in Figure 8b was also smaller than that of the other three samples. It was clear to see that the diameter of arc radius followed in the order of $D-CN < M-CN < T-CN < U-CN$, which agrees well with the PL spectra.

As mentioned above, the photoelectric properties have little effect on the photocatalytic reduction of Cr(VI). Although having the widest bandgap, U-CN displays the best photocatalytic reduction performance. T-CN has the highest white light absorption and much higher charge separation efficiency, but it displays the lowest photocatalytic reduction activity.

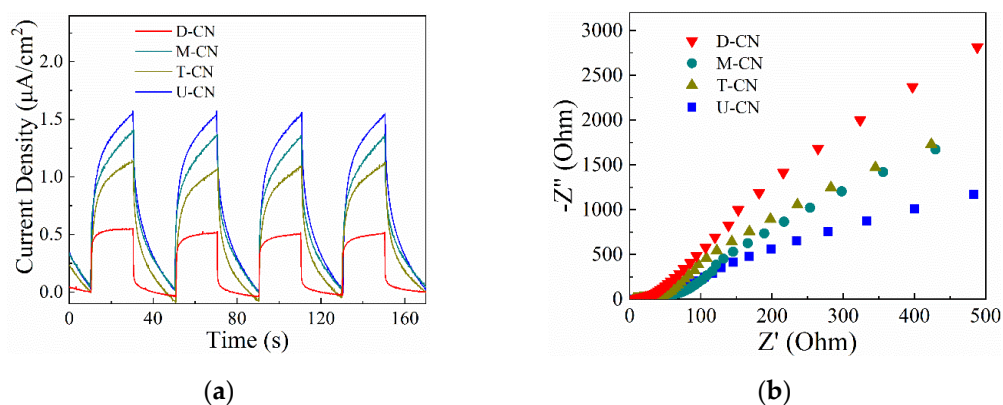


Figure 8. (a) Photocurrent response; (b) EIS Nyquist plots of D—CN, M—CN, T—CN, U—CN.

2.4. Possible Reaction Mechanism

Previous studies have shown that the photocatalytic reduction of Cr (VI) on the surface of $g\text{-C}_3\text{N}_4$ occurs via a direct or indirect reduction of photogenerated electrons. The trapping of photogenerated electrons by O_2 is critical for Cr (VI) reduction in the reduction process [3,29,44,45]. To investigate the role of O_2 on the photocatalytic reduction of Cr (VI) over U-CN in the presence of citric acid, the comparison experiments were carried out in different gas atmospheres. It is found from Figure 9a that the photocatalytic reduction of Cr(VI) over U-CN in the N_2 atmosphere was obviously enhanced, whereas the photocatalytic reduction of Cr(VI) over U-CN in O_2 atmosphere was depressed to some extent. The results indicate that O_2 is involved in the photocatalytic reduction of Cr (VI) over U-CN. ESR technique was further employed to measure the reactive species generated during photocatalysis. As shown in Figure 9b, signals of $\text{DMPO}\cdot\text{O}_2^-$ could be detected in methanolic suspension of U-CN under white light irradiation, reflecting that O_2^- is generated via electron transfer from conduction band of U-CN to the dissolved molecular oxygen under white light illumination. Thus, it can be concluded that in the photocatalytic reduction system, Cr (VI) is direct reduced by photogenerated electrons over U-CN, whereas O_2 in the solution competes with Cr(VI) for the photogenerated electrons, inhibiting Cr(VI) reduction. While citric acid acts as sacrificial agent of reactive oxygen species in the system, avoiding the Cr(III) re-oxidation, while the surplus electrons will participate in the reaction of Cr(VI) reduction or trapped by O_2 to form O_2^- (Figure 10) [46,47].

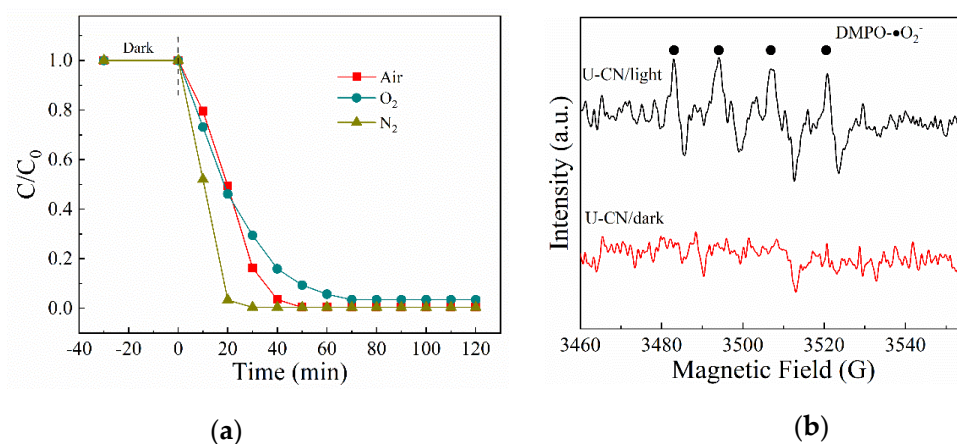


Figure 9. (a) Photocatalytic reduction of Cr(VI) in air and N_2 ambient; (b) ESR spectrum of O_2^- .

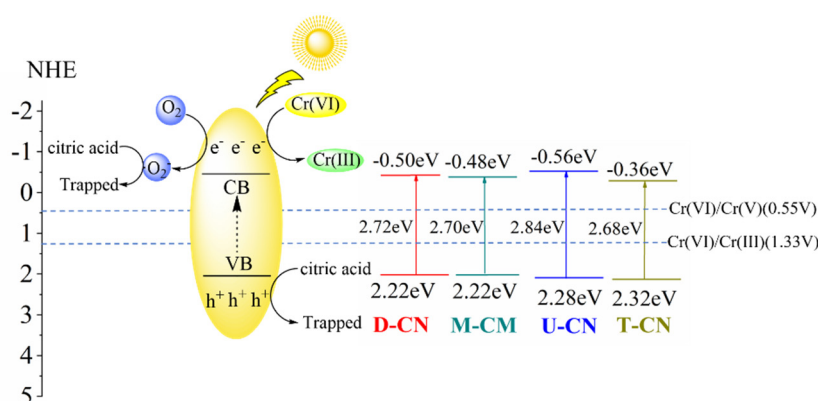


Figure 10. Proposed mechanism for photocatalytic reduction of Cr(VI) over U-CN.

3. Materials and Methods

3.1. Materials and Instruments

Melamine, dicyandiamide, thiourea, urea, potassium dichromate ($K_2Cr_2O_7$), acetone, sulfuric acid (H_2SO_4), phosphoric acid (H_3PO_4), diphenyl carbonyl hydrazine, sodium hydroxide (NaOH), methyl alcohol, oxalic acid, formic acid, citric acid, and tartaric acid were all analytical grade and obtained from Chron Chemical Reagent Co., Ltd. (Chengdu, China.) Furthermore, 5,5-dimethyl-1-pyrroline N-oxide (DMPO) was supplied by the Aladdin Industrial Corporation (Shanghai, China). All the reagents were analytically pure and the solutions were prepared using ultrapure water.

3.2. Preparation of Graphitic Carbon Nitride ($g-C_3N_4$)

The $g-C_3N_4$ samples were synthesized by a thermal polymerization method using dicyandiamide, melamine, thiourea, and urea as precursors. Typically, 10 g of the precursor powder was put into an alumina crucible and heated at $5^\circ C/min$ up to $550^\circ C$ for 3 h in a covered muffle furnace. After the crucible cooling to room temperature, four products were collected and ground into powder. The obtained products were named as D-CN, M-CN, T-CN, and U-CN, respectively (Figure S1, Supplementary Materials).

3.3. Photocatalytic Experiments

The photocatalytic activity of the synthesized samples for the removal of Cr(VI) was evaluated under white light provided by a Xe light with the power of 300 W (Perfectlight). At room temperature a certain amount of $g-C_3N_4$ was suspended into 150 mL aqueous solution of Cr(VI) (50 mg/L) with the addition of citric acid (0.9 mM). The solution pH was adjusted to 3 by H_2SO_4 (1 M) or NaOH (1 M). Prior to irradiation, the suspension was ultrasonicated for 10 min and stirred in the dark for 30 min to establish the adsorption-desorption equilibrium. Subsequently, the light source was switched on. During the illumination process, a certain amount of the solution was taken at a predetermined time interval and filtered through a $0.45 \mu m$ filter. The Cr(VI) concentration in the supernatant was determined at 540 nm using the diphenylcarbazide (DPC) method by a spectrophotometer at the characteristic wavelength of 540 nm.

3.4. Characterization

X-ray diffraction (XRD) patterns were examined using X-ray diffractometer (Panalytical X'Pert-pro MPD, Almelo, The Netherlands) with Cu $K\alpha$ radiation source ($\lambda = 1.54056 \text{ \AA}$) in the range of 10° – 60° . The Fourier transform infrared spectra were measured using an infrared spectrometer (Nicolet iS 10, Madison, WI, USA) with KBr pellets. The morphology of the sample was studied using a scanning electron microscope (Hitachi S-4700, Tokyo, Japan). Thermogravimetry (TG) of the samples was analyzed by TA synchronous thermal analyzer (TA Q600, New Castle, USA). The surface area was calculated using the multi-point BET (Quantachrome NOVA 2000e, Boynton Beach, USA) method. X-ray photo-

electron spectroscopy (XPS) was performed using an X-ray photoelectron (ThermoFischer ESCALAB 250Xi, Waltham, MA, USA) spectrometer with Al monochrome ($h\nu = 1486.6$ eV) as the X-ray source. The zeta potential of the prepared sample was measured at 293 K using a zeta potential analyzer (Malvern, Zetasizer Nano ZS90, Worcestershire, UK). The UV-vis diffuse reflectance spectra (UV-DRS) were measured on a UV-vis spectrometer (Shimadzu UV-2600, Kyoto, Japan). The photoluminescence (PL) spectra of the samples were recorded by using a fluorescence spectrophotometer (Hitachi F-7100, Tokyo, Japan). The ESR spectra were recorded on a ESR spectrometer (Bruker EMX plus X-band CW, Rheinstetten, Germany) using DMPO as a spin trap agent at room temperature.

The photoelectrochemical measurements were applied in a standard three-electrode cell with an electrochemical workstation (CHI770E, CHN). A Pt and Ag/AgCl (saturated KCl) electrode were chosen as counter and reference electrode, respectively. ITO coated with the prepared catalyst served as the working electrode. The working electrodes were prepared as follows: 5 mg of the as-obtained photocatalyst was suspended in a mixed solution (10 μ L of 5% nafion and 2 mL of ethanol) with ultrasound. After that, 100 μ L of the obtained suspension was drop-coated on the ITO glass (10 mm \times 10 mm), and dried in the air to completely eliminate water. Additionally, 0.1 M Na₂SO₄ was used as electrolyte.

4. Conclusions

In this study, g-C₃N₄ composites are synthesized via a facile polymerized method with four different precursors (i.e., melamine, dicyandiamide, thiourea, and urea). It was found that the type of precursors has a significant impact on the morphology and structure of g-C₃N₄ and further affects the performance of photocatalytic reduction of Cr(VI). Urea-derived U-CN with nanosheet morphology, large specific surface area, and high occupancies of surface amine groups exhibit superior photocatalytic activity. These results demonstrate that large surface area and high surface amine groups can provide more catalytically active sites. This work confirms the effect of surface properties on the photocatalytic activity of g-C₃N₄ and provides a theoretical and technical foundation for the construction of practical and high-efficiency photocatalysts based on g-C₃N₄.

Supplementary Materials: The following are available online. Figure S1: g-C₃N₄ photocatalysts prepared by different precursors, Figure S2: (a) Photocatalytic removal of Cr(VI) over g-C₃N₄ photocatalysts prepared by different precursors (b) Photodegradation kinetic constants of the as-prepared photocatalysts under white light and visible light, Figure S3: Effect of hole scavengers on photocatalytic Cr(VI) reduction, Figure S4: Effect of Cr(VI) initial concentration on photocatalytic Cr(VI) reduction.

Author Contributions: Data curation J.L.; formal analysis, J.L.; methodology, J.L.; project administration, Y.M. and J.W.; resources, C.J. and J.W.; supervision, J.W.; validation, J.L.; writing—original draft, J.L.; writing—review and editing, C.J. All authors have read and agreed to the published version of the manuscript.

Funding: This work was funded by the Department of Science and Technology of Sichuan Province (No.2020YJ0061) and Innovation Spark Project of Sichuan University (No. 2019SCUH0009).

Institutional Review Board Statement: Not applicable.

Informed Consent Statement: Not applicable.

Data Availability Statement: Data are contained within the article.

Acknowledgments: We appreciate the support of the SEM imaging by the Institute of New Energy and Low Carbon Technology of Sichuan University.

Conflicts of Interest: The authors declare no conflict of interest.

Sample Availability: The samples are available from the authors.

References

1. Huang, X.; Hou, X.; Song, F.; Zhao, J.; Zhang, L. Facet-Dependent Cr(VI) Adsorption of Hematite Nanocrystals. *Environ. Sci. Technol.* **2016**, *50*, 1964–1972. [[CrossRef](#)] [[PubMed](#)]
2. Li, K.; Huang, Z.; Zhu, S.; Luo, S.; Yan, L.; Dai, Y.; Guo, Y.; Yang, Y. Removal of Cr(VI) from water by a biochar-coupled g-C₃N₄ nanosheets composite and performance of a recycled photocatalyst in single and combined pollution systems. *Appl. Catal. B Environ.* **2019**, *243*, 386–396. [[CrossRef](#)]
3. Dong, G.; Zhang, L. Synthesis and Enhanced Cr(VI) Photoreduction Property of Formate Anion Containing Graphitic Carbon Nitride. *J. Phys. Chem. C* **2013**, *117*, 4062–4068. [[CrossRef](#)]
4. Jiang, B.; Liu, Y.; Zheng, J.; Tan, M.; Wang, Z.; Wu, M. Synergetic Transformations of Multiple Pollutants Driven by Cr(VI)–Sulfite Reactions. *Environ. Sci. Technol.* **2015**, *49*, 12363–12371. [[CrossRef](#)]
5. Liu, F.; Yu, J.; Tu, G.; Qu, L.; Xiao, J.; Liu, Y.; Wang, L.; Lei, J.; Zhang, J. Carbon nitride coupled Ti-SBA15 catalyst for visible-light-driven photocatalytic reduction of Cr(VI) and the synergistic oxidation of phenol. *Appl. Catal. B* **2017**, *201*, 1–11. [[CrossRef](#)]
6. Meichtry, J.M.; Colbeau-Justin, C.; Custo, G.; Litter, M.I. Preservation of the photocatalytic activity of TiO₂ by EDTA in the reductive transformation of Cr(VI). Studies by Time Resolved Microwave Conductivity. *Catal. Today* **2014**, *224*, 236–243. [[CrossRef](#)]
7. Wan, Z.; Zhang, G.; Wu, X.; Yin, S. Novel visible-light-driven Z-scheme Bi₁₂GeO₂₀/g-C₃N₄ photocatalyst: Oxy-gen-induced pathway of organic pollutants degradation and proton assisted electron transfer mechanism of Cr(VI) reduction. *Appl. Catal. B* **2017**, *207*, 17–26. [[CrossRef](#)]
8. Wang, F.; Chen, P.; Feng, Y.; Xie, Z.; Liu, Y.; Su, Y.; Zhang, Q.; Wang, Y.; Yao, K.; Lv, W.; et al. Facile synthesis of N-doped carbon dots/g-C₃N₄ photocatalyst with enhanced visible-light photocatalytic activity for the degradation of indomethacin. *Appl. Catal. B* **2017**, *207*, 103–113. [[CrossRef](#)]
9. Li, Y.; Zhang, C.; Shuai, D.; Naraginti, S.; Wang, D.; Zhang, W. Visible-light-driven photocatalytic inactivation of MS2 by metal-free g-C₃N₄: Virucidal performance and mechanism. *Water Res.* **2016**, *106*, 249–258. [[CrossRef](#)] [[PubMed](#)]
10. Zhang, H.; Guo, L.-H.; Zhao, L.; Wan, B.; Yang, Y. Switching Oxygen Reduction Pathway by Exfoliating Graphitic Carbon Nitride for Enhanced Photocatalytic Phenol Degradation. *J. Phys. Chem. Lett.* **2015**, *6*, 958–963. [[CrossRef](#)]
11. Wang, X.; Pehkonen, A.S.O.; Ray, A. Removal of Aqueous Cr(VI) by a Combination of Photocatalytic Reduction and Coprecipitation. *Ind. Eng. Chem. Res.* **2004**, *43*, 1665–1672. [[CrossRef](#)]
12. Mishra, A.; Mehta, A.; Kainth, S.; Basu, S. A comparative study on the effect of different precursors for synthesis and efficient photocatalytic activity of g-C₃N₄/TiO₂/bentonite nanocomposites. *J. Mater. Sci.* **2018**, *53*, 13126–13142. [[CrossRef](#)]
13. Pham, T.; Shin, E.W. Influence of g-C₃N₄ Precursors in g-C₃N₄/NiTiO₃ Composites on Photocatalytic Behavior and the Interconnection between g-C₃N₄ and NiTiO₃. *Langmuir* **2018**, *34*, 13144–13154. [[CrossRef](#)]
14. Lee, H.L.; Sofer, Z.; Mazánek, V.; Luxa, J.; Chua, C.K.; Pumera, M. Graphitic carbon nitride: Effects of various precursors on the structural, morphological and electrochemical sensing properties. *Appl. Mater. Today* **2017**, *8*, 150–162. [[CrossRef](#)]
15. Tian, C.; Zhao, H.; Mei, J.; Yang, S. Cost-Efficient Graphitic Carbon Nitride as an Effective Photocatalyst for Antibiotic Degradation: An Insight into the Effects of Different Precursors and Coexisting Ions, and Photocatalytic Mechanism. *Chem. Asian J.* **2019**, *14*, 162–169. [[CrossRef](#)] [[PubMed](#)]
16. Nguyen, T.K.A.; Pham, T.; Nguyen-Phu, H.; Shin, E.W. The effect of graphitic carbon nitride precursors on the photocatalytic dye degradation of water-dispersible graphitic carbon nitride photocatalysts. *Appl. Surf. Sci.* **2021**, *537*, 148027. [[CrossRef](#)]
17. Guan, C.; Jiang, J.; Pang, S.; Chen, X.; Webster, R.D.; Lim, T. Facile synthesis of pure g-C₃N₄ materials for peroxymonosulfate activation to degrade bisphenol A: Effects of precursors and annealing ambience on catalytic oxidation. *Chem. Eng. J.* **2020**, *387*, 123726. [[CrossRef](#)]
18. Majdoub, M.; Anfar, Z.; Amedlous, A. Emerging Chemical Functionalization of g-C₃N₄: Covalent/Noncovalent Modifications and Applications. *ACS Nano* **2020**, *14*, 12390–12469. [[CrossRef](#)]
19. Martha, S.; Nashim, A.; Parida, K.M. Facile synthesis of highly active g-C₃N₄ for efficient hydrogen production under visible light. *J. Mater. Chem. A* **2013**, *1*, 7816–7824. [[CrossRef](#)]
20. Martin, D.J.; Qiu, K.; Shevlin, S.A.; Handoko, A.D.; Chen, X.; Guo, Z.; Tang, J. Highly Efficient Photocatalytic H₂Evolution from Water using Visible Light and Structure-Controlled Graphitic Carbon Nitride. *Angew. Chem. Int. Ed.* **2014**, *53*, 9240–9245. [[CrossRef](#)]
21. Ismael, M.; Wu, Y.; Taffa, D.H.; Bottke, P.; Wark, M. Graphitic carbon nitride synthesized by simple pyrolysis: Role of precursor in photocatalytic hydrogen production. *New J. Chem.* **2019**, *43*, 6909–6920. [[CrossRef](#)]
22. Ibad, M.F.; Kosslick, H.; Tamm, J.W.; Frank, M.; Schulz, A. Impact of the crystallinity of mesoporous polymeric graphitic carbon nitride on the photocatalytic performance under UV and visible light. *Microporous Mesoporous Mater.* **2017**, *254*, 136–145. [[CrossRef](#)]
23. Feng, D.; Cheng, Y.; He, J.; Zheng, L.; Shao, D.; Wang, W.; Wang, W.; Lu, F.; Dong, H.; Liu, H.; et al. Enhanced photocatalytic activities of g-C₃N₄ with large specific surface area via a facile one-step synthesis process. *Carbon* **2017**, *125*, 454–463. [[CrossRef](#)]
24. Yang, S.; Gong, Y.; Zhang, J.; Zhan, L.; Ma, L.; Fang, Z.; Vajtai, R.; Wang, X.; Ajayan, P.M. Exfoliated Graphitic Carbon Nitride Nanosheets as Efficient Catalysts for Hydrogen Evolution Under Visible Light. *Adv. Mater.* **2013**, *25*, 2452–2456. [[CrossRef](#)] [[PubMed](#)]

25. Chen, D.; Liu, J.; Jia, Z.; Fang, J.; Yang, F.; Tang, Y.; Wu, K.; Liu, Z.; Fang, Z. Efficient visible-light-driven hydrogen evolution and Cr(VI) reduction over porous P and Mo co-doped g-C₃N₄ with feeble N vacancies photocatalyst. *J. Hazard. Mater.* **2019**, *361*, 294–304. [[CrossRef](#)]
26. Yang, Y.; Yang, X.; Leng, D.; Wang, S.; Zhang, W. Fabrication of g-C₃N₄/SnS₂/SnO₂ nanocomposites for promoting photo-catalytic reduction of aqueous Cr(VI) under visible light. *Chem. Eng. J.* **2018**, *335*, 491–500. [[CrossRef](#)]
27. Liu, Q.; Chen, T.; Guo, Y.; Zhang, Z.; Fang, X. Ultrathin g-C₃N₄ nanosheets coupled with carbon nanodots as 2D/0D composites for efficient photocatalytic H₂ evolution. *Appl. Catal. B* **2016**, *193*, 248–258. [[CrossRef](#)]
28. Yuan, J.; Liu, X.; Tang, Y.; Zeng, Y.; Wang, L.; Zhang, S.; Cai, T.; Liu, Y.; Luo, S.; Pei, Y.; et al. Positioning cyanamide defects in g-C₃N₄: Engineering energy levels and active sites for superior photocatalytic hydrogen evolution. *Appl. Catal. B Environ.* **2018**, *237*, 24–31. [[CrossRef](#)]
29. Wei, H.; Zhang, Q.; Zhang, Y.; Yang, Z.; Zhu, A.; Dionysiou, D. Enhancement of the Cr(VI) adsorption and photocatalytic reduction activity of g-C₃N₄ by hydrothermal treatment in HNO₃ aqueous solution. *Appl. Catal. A Gen.* **2016**, *521*, 9–18. [[CrossRef](#)]
30. Zhang, Y.; Liu, J.; Wu, G.; Chen, W. Porous graphitic carbon nitride synthesized via direct polymerization of urea for efficient sunlight-driven photocatalytic hydrogen production. *Nanoscale* **2012**, *4*, 5300–5303. [[CrossRef](#)]
31. Devthade, V.; Kulhari, D.; Umare, S.S. Role of precursors on photocatalytic behavior of graphitic carbon nitride. *Mater. Today Proc.* **2018**, *5*, 9203–9210. [[CrossRef](#)]
32. Lin, Z.; Waller, G.; Liu, Y.; Liu, M.; Wong, C.-P. Facile Synthesis of Nitrogen-Doped Graphene via Pyrolysis of Graphene Oxide and Urea, and its Electrocatalytic Activity toward the Oxygen-Reduction Reaction. *Adv. Energy Mater.* **2012**, *2*, 884–888. [[CrossRef](#)]
33. Zheng, Y.; Zhang, Z.; Li, C. A comparison of graphitic carbon nitrides synthesized from different precursors through pyrolysis. *J. Photochem. Photobiol. A Chem.* **2017**, *332*, 32–44. [[CrossRef](#)]
34. Liu, J.; Zhang, T.; Wang, Z.; Dawson, G.; Chen, W. Simple pyrolysis of urea into graphitic carbon nitride with recyclable adsorption and photocatalytic activity. *J. Mater. Chem.* **2011**, *21*, 14398–14401. [[CrossRef](#)]
35. Jiang, L.; Yuan, X.; Zeng, G.; Chen, X.; Wu, Z.; Liang, J.; Zhang, J.; Wang, H.; Wang, H. Phosphorus- and Sulfur-Codoped g-C₃N₄: Facile Preparation, Mechanism Insight, and Application as Efficient Photocatalyst for Tetracycline and Methyl Orange Degradation under Visible Light Irradiation. *ACS Sustain. Chem. Eng.* **2017**, *5*, 5831–5841. [[CrossRef](#)]
36. Fu, J.; Zhu, B.; Jiang, C.; Cheng, B.; You, W.; Yu, J. Hierarchical Porous O-Doped g-C₃N₄ with Enhanced Photocatalytic CO₂ Reduction Activity. *Small* **2017**, *13*, 1603938. [[CrossRef](#)] [[PubMed](#)]
37. Hu, C.; Tsai, W.-F.; Wei, W.-H.; Lin, K.-Y.A.; Liu, M.-T.; Nakagawa, K. Hydroxylation and sodium intercalation on g-C₃N₄ for photocatalytic removal of gaseous formaldehyde. *Carbon* **2021**, *175*, 467–477. [[CrossRef](#)]
38. Zhu, B.; Xia, P.; Ho, W.; Yu, J. Isoelectric point and adsorption activity of porous g-C₃N₄. *Appl. Surf. Sci.* **2015**, *344*, 188–195. [[CrossRef](#)]
39. Wang, X.L.; Fang, W.Q.; Liu, W.; Jia, Y.; Jing, D.; Wang, Y.; Yang, L.; Gong, X.; Yao, Y.; Yang, H.G.; et al. Brønsted base site engineering of graphitic carbon nitride for enhanced photocatalytic activity. *J. Mater. Chem. A* **2017**, *5*, 19227–19236. [[CrossRef](#)]
40. Patnaik, S.; Das, K.K.; Mohanty, A.; Parida, K. Enhanced photocatalytic reduction of Cr(VI) over polymer-sensitized g-C₃N₄/ZnFe₂O₄ and its synergism with phenol oxidation under visible light irradiation. *Catal. Today* **2018**, *315*, 52–66. [[CrossRef](#)]
41. Wang, H.; Yuan, X.; Wu, Y.; Zeng, G.; Chen, X.; Leng, L.; Wu, Z.; Jiang, L.; Li, H. Facile synthesis of amino-functionalized titanium metal-organic frameworks and their superior visible-light photocatalytic activity for Cr(VI) reduction. *J. Hazard. Mater.* **2015**, *286*, 187–194. [[CrossRef](#)] [[PubMed](#)]
42. Wang, C.-C.; Du, X.-D.; Li, J.; Guo, X.-X.; Wang, P.; Zhang, J. Photocatalytic Cr(VI) reduction in metal-organic frameworks: A mini-review. *Appl. Catal. B Environ.* **2016**, *193*, 198–216. [[CrossRef](#)]
43. Liu, W.; Li, Y.; Liu, F.; Jiang, W.; Zhang, D.; Liang, J. Visible-light-driven photocatalytic degradation of diclofenac by carbon quantum dots modified porous g-C₃N₄: Mechanisms, degradation pathway and DFT calculation. *Water Res.* **2019**, *151*, 8–19. [[CrossRef](#)] [[PubMed](#)]
44. Yi, X.; Ma, S.; Du, X.; Zhao, C.; Fu, H.; Wang, P.; Wang, C. The facile fabrication of 2D/3D Z-scheme g-C₃N₄/UiO-66 heterojunction with enhanced photocatalytic Cr(VI) reduction performance under white light. *Chem. Eng. J.* **2019**, *375*, 121944. [[CrossRef](#)]
45. Yuan, F.; Sun, Z.; Li, C.; Tan, Y.; Zhang, X.; Zheng, S. Multi-component design and in-situ synthesis of visible-light-driven SnO₂/g-C₃N₄/diatomite composite for high-efficient photoreduction of Cr(VI) with the aid of citric acid. *J. Hazard. Mater.* **2020**, *396*, 122694. [[CrossRef](#)] [[PubMed](#)]
46. Chen, Y.; Liu, Z.; Wang, Z.; Xue, M.; Zhu, X.; Tao, T. Photodegradation of propranolol by Fe(III)-citrate complexes: Kinetics, mechanism and effect of environmental media. *J. Hazard. Mater.* **2011**, *194*, 202–208. [[CrossRef](#)] [[PubMed](#)]
47. Marinho, B.A.; Cristóvão, R.O.; Loureiro, J.M.; Boaventura, R.A.; Vilar, V.J. Solar photocatalytic reduction of Cr(VI) over Fe(III) in the presence of organic sacrificial agents. *Appl. Catal. B Environ.* **2016**, *192*, 208–219. [[CrossRef](#)]